A Nail-size Piezoelectric Energy Harvesting System Integrating a MEMS Transducer and a CMOS SSHI Circuit

Sijun Du, *Member, IEEE,* Yu Jia, *Senior Member, IEEE,* Chun Zhao, *Member, IEEE,* Gehan A. J. Amaratunga and Ashwin A. Seshia, *Senior Member, IEEE*

***Abstract*—Piezoelectric vibration energy harvesting has drawn much interest to power distributed wireless sensor nodes for Internet of Things (IoT) applications where ambient kinetic energy is available. For certain applications, the harvesting system should be small and able to generate sufficient output power. Standard rectification topologies such as the full-bridge rectifier are typically inefficient when adapted to power conditioning from miniaturized harvesters. Therefore, active rectification circuits have been researched to improve overall power conversion efficiency, and meet both the output power and miniaturization requirements while employing a MEMS harvester. In this paper, a MEMS piezoelectric energy harvester is designed and co-integrated with an active synchronized switch harvesting on inductor (SSHI) rectification circuit designed in a CMOS process to achieve high output power for system miniaturization. The system is fully integrated on a nail-size board, which is ready to provide a stable DC power for low-power mini sensors. A MEMS energy harvester of $0.005\,\mathrm{cm}^3$ size, co-integrated with the CMOS conditioning circuit, outputs a peak rectified DC power of $40.6\,\mu\mathrm{W}$ and achieves a record DC power density of $8.12\,\mathrm{mW/cm}^3$ when compared to state-of-the-art harvesters.**

***Index Terms*—Keywords: Energy harvesting, MEMS, energy conversion, integrated circuits, piezoelectric transducer, rectification, power conditioning, SSHI, system miniaturization, Internet of Things (IoT), wireless sensor networks (WSN), renewable energy.**

I. Introduction

The Internet of Things (IoT) continues to expand in both number and variety and the deployment of wireless sensor networks (WSN) has been developed to interconnect the physical and cyber worlds. Harvesting ambient vibration energy for self-powered wireless sensors has received much research interest in recent years [1]–[11]. Among the various vibration energy harvesters, piezoelectricity has been widely used due to its high power density and integration with conventional CMOS circuits [12]–[14]. During real-world implementations, miniaturization of the entire integrated energy harvesting system has been one of the key challenges. In addition, the output power from miniaturized harvesters also need to meet requirements to continuously power the sensors and periodically send wireless data [15]–[17]. However, output power and the generated voltage from a miniaturized piezoelectric transducer (PT) are usually much lower than macroscopic PTs. Hence an efficient interface circuit is needed to increase the power extraction efficiency while ensuring that miniaturization benefits are not compromised [18], [19]. A complete vibration energy harvesting system consists of a PT and an interface circuit, which rectifies, manages and regulates the harvested energy to provide a stable DC power supply for load electronics [20]. An system block diagram is shown in Fig. 1a and a miniaturized energy harvesting prototype is fabricated and shown in Fig. 1b. The size of the prototype is $1\,\mathrm{cm} \times 1\,\mathrm{cm} \times 0.4\,\mathrm{cm}$ and it consists of a cantilevered MEMS (Microelectromechanical Systems) PT, a CMOS interface circuit, an inductor and several capacitors.

In order to rectify the raw power generated from a PT, a full-bridge rectifier (FBR) is widely employed due to its simplicity and stability [20], [21]. Fig. 2a shows the circuit diagram of a full-bridge rectifier and the associated waveforms. The PT while vibrating is modeled as a current source I_P in parallel with a capacitor C_P. Some publications include a resistor R_P in parallel; however, R_P is ignored in this manuscript for simplicity since its resistance is much higher than the impedance of C_P at the resonant frequency. Power rectification is typically achieved by a FBR, which consists of four diodes, into a storage capacitor C_S. The signal V_{PT} in the waveform is the voltage across the PT. From the waveform, it can be seen that V_{PT} needs to attain either $V_S + 2V_D$ or $-(V_S + 2V_D)$ in order to transfer energy into C_S, where V_D is the forward voltage drop of the diodes. Hence, V_{PT} needs to be flipped between these two voltage levels for each half period and the energy used to flip V_{PT} is wasted, which is illustrated as fully shaded areas in the I_P graph. Assuming the open-circuit voltage amplitude generated from the PT is V_{OC}, the condition for a FBR to start operating is:

$$V_{OC} > V_S + 2V_D \tag{1}$$

If equation (1) is not satisfied, all generated energy is wasted (internally dissipated in the harvester front-end). Even if it is marginally satisfied, most of energy is wasted and the power

S. Du is with the Department of Engineering, University of Cambridge, Cambridge, CB2 1PZ, U.K., and also with the Department of Electrical Engineering and Computer Sciences, University of California, Berkeley, CA, 94720, U.S.A. (e-mail: sijundu@hotmail.com; sijun@eecs.berkeley.edu).

Y. Jia is with Mechanical Engineering and Design, Aston University, Birmingham, B4 7ET, U.K.

G. A. J. Amaratunga and A. A. Seshia are with the Department of Engineering, University of Cambridge, Cambridge, CB2 1PZ, U.K.

C. Zhao is with the Department of Engineering, University of Cambridge, Cambridge, CB2 1PZ, UK, and also with the Center for Gravitational Experiments, Huazhong University of Science and Technology, Wuhan, 430074, China.

Correspondence and requests for materials should be addressed to Ashwin A. Seshia (e-mail: aas41@cam.ac.uk).

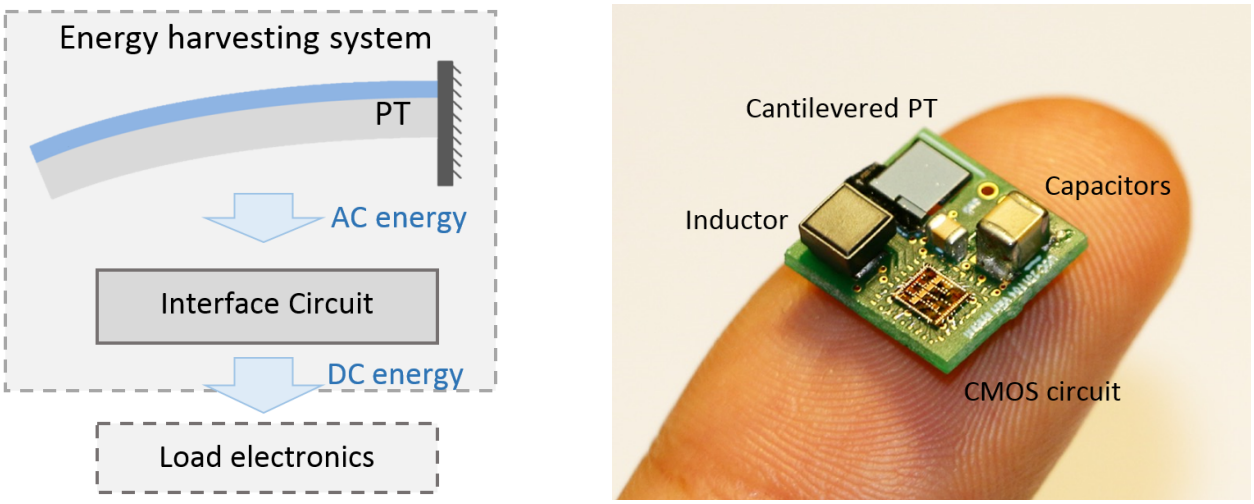

(a) (b)

Fig. 1: System block diagram and a fabricated prototype of a complete vibration energy harvesting system (a) system block diagram (b) prototype of size $1\,\mathrm{cm} \times 1\,\mathrm{cm} \times 0.4\,\mathrm{cm}$.

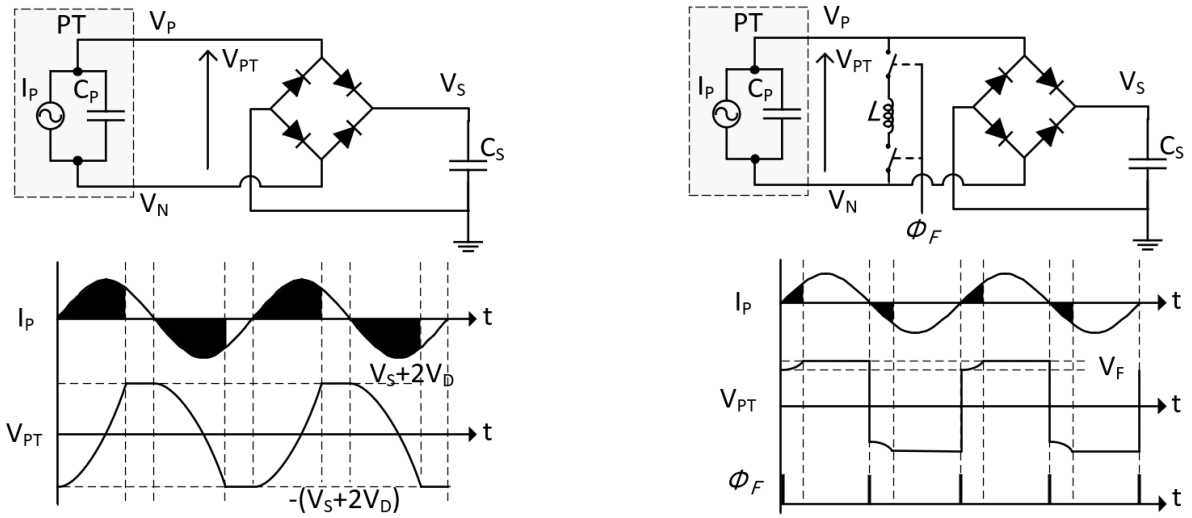

(a) (b)

Fig. 2: (a) Full-bridge rectifier and associated waveforms. (b) SSHI circuit and associated waveforms.

efficiency is extremely low in this case. A FBR may have acceptable power efficiency while employing a macroscopic PT, which can generate relatively high open-circuit voltage. However, MEMS (microelectromechanical system) energy harvesters have been widely employed for miniaturization in the past decade [22]–[25]. if a MEMS PT is employed, the generated voltage can be much lower. For example, assuming $V_S = 3\,\mathrm{V}$ and $V_D = 0.3\,\mathrm{V}$, V_{OC} needs to attain $3.6\,\mathrm{V}$ (or $7.2\,\mathrm{V}$ peak-to-peak) to be able to turn on the diodes, which can be difficult to achieve for a MEMS PT at low vibration levels. Therefore, in order to increase the extracted power, many active interface circuits have been proposed in recent years [26]–[41]. Most of these circuits employ inductors and synchronous switches to perform nonlinear energy extraction, such as synchronized switch harvesting on inductor (SSHI), synchronous electric charge extraction (SECE), etc [42]–[51].

Most of previous works are either focused on power-conditioning circuits or PTs; however, there are few works targeting at complete-system integration and miniaturization. This is mainly because miniaturized MEMS PTs usually have low output power and voltage, which make the interface circuits difficult to operate correctly to extract energy and to be self-sustained. Besides, miniaturized MEMS PTs usually have high resonance frequencies (in kHz range), where are not suitable for most environmental vibration sources (usually below 500 Hz). In this paper, a MEMS PT is fabricated and integrated with an SSHI interface circuit implemented in a $0.35\,\mu\mathrm{m}$ CMOS process. The SSHI interface circuit significantly increases the rectified power from the PT and the MEMS device is designed with a low resonance frequency (199 Hz), which is comparable with most of state-of-the-art devices with larger sizes. In addition, the high integration of

the whole system realizes a nail sized design ($\sim 0.4\,\mathrm{cm}^3$), suitable for many applications with miniaturization considerations, such as self-powered wireless sensors for Internet of Things (IoT) or biomedical implants. The rest of this paper is organized as follows: Section II models the system and provides output power analysis with comparisons to a passive FBR. Detailed circuit implementations and mechanical characterizations are provided in Section III and Section IV, respectively. Measured results and comparisons with state-of-the-art vibration energy harvesters are provided in Section V and a conclusion is provided in the last section.

II. Output power modeling

A. Full-bridge rectifier

This section models the full-bridge rectifier (FBR) and analyzes the the DC power transferred into the capacitor C_S. The circuit diagram of a FBR is shown in Fig. 2a. While the PT is vibrating, the current source can be expressed as $I_P = I_0 \sin(\omega t)$, where ω is the excitation frequency. Hence, the charge generated in a half period is:

$$Q_{total} = \int_0^{\frac{T}{2}} I_0 \sin \omega t \mathrm{d}t = \frac{2I_0}{\omega} \tag{2}$$

If the PT is in an open circuit, the open-circuit zero-peak amplitude can be calculated as:

$$V_{OC} = \frac{1}{2}\frac{Q_{total}}{C_P} = \frac{I_0}{\omega C_P} \tag{3}$$

As a certain amount of charge is wasted to flip V_{PT} between $V_S + 2V_D$ and $-(V_S + 2V_D)$, the remaining charge transferred into C_S can be expressed as:

$$Q_{FBR} = Q_{total} - 2(V_S + 2V_D)C_P \tag{4}$$

Hence, the energy flowing into C_S is:

$$E_{FBR} = V_S Q_{FBR} = 2C_P V_S(V_{OC} - V_S - 2V_D) \tag{5}$$

Therefore, the extracted power in this half period is:

$$P_{FBR} = \frac{E_{FBR}}{T/2} = 4C_P V_S f_P(V_{OC} - V_S - 2V_D) \tag{6}$$

It can be found that the maximum power point (MPP) of P_{FBR} is obtained when $V_S = \frac{V_{OC}}{2} - V_D$. The peak power transferred to C_S is:

$$P_{FBR(max)} = 4C_P f_P(\frac{V_{OC}}{2} - V_D)^2 \tag{7}$$

While using active diodes built with low V_{TH} transistors, such as active diodes introduced in [52], the forward voltage drop of the diodes V_D can be ignored. In this case, the peak power can be rewritten as:

$$P_{FBR(max)} = C_P f_P V_{OC}^2 \tag{8}$$

B. SSHI circuit

In order to minimize the wasted charge due to flipping the voltage V_{PT} across the PT, the synchronized switch harvesting on inductor (SSHI) interface circuit has been proposed and implemented to increase the power extraction efficiency [49]. The circuit diagram and the associated waveforms are shown in Fig. 2b. In the SSHI rectifier, an inductor is employed to form an RLC oscillation loop to flip V_{PT}. The pulse signal ϕ_F is synchronously generated and its pulsewidth is adjusted to be a half-pseudo period of the RLC system. During the pulse ϕ_F, V_{PT} is flipped with a loss V_F, which can be expressed as:

$$V_F = (V_S + 2V_D)(1 - e^{-\frac{\pi}{\sqrt{\frac{4L}{R^2C_P} - 1}}}) = (V_S + 2V_D)\eta_F \tag{9}$$

where the threshold V_F is illustrated in Fig. 2b, which represents the voltage loss after one flip. R is the total resistance in the RLC loop, which consists of the DC resistance of the inductor, the ON resistance of switches and other parasitic resistance in wires and contacts. η_F is the voltage loss ratio between 0 and 1 and it is expressed as $\eta_F = 1 - e^{-\frac{\pi}{\sqrt{\frac{4L}{R^2C_P} - 1}}}$. As V_F is the voltage loss after one flip in a half period, the remaining charge flowing into C_S is:

$$Q_{S(SSHI)} = Q_{total} - C_P V_F = C_P(2V_{OC} - V_F) \tag{10}$$

Hence, the extracted power is:

$$\begin{aligned} P_{SSHI} &= 2f_P C_P V_S(2V_{OC} - V_F) \\ &= 2f_P C_P V_S(2V_{OC} - (V_S + 2V_D)\eta_F) \end{aligned} \tag{11}$$

The power attains its MPP when $V_S = \frac{V_{OC}}{\eta_F} - V_D$ and the maximum power can be calculated as:

$$P_{SSHI(max)} = 2C_P f_P \eta_F(\frac{V_{OC}}{\eta_F} - V_D)^2 = \frac{2}{\eta_F} C_P f_P V_{OC}^2 \tag{12}$$

where V_D is ignored. Comparing the MPP values in equations (8) and (12), the performance improvement of using a SSHI circuit compared to a FBR can be expressed as:

$$\frac{P_{SSHI}}{P_{FBR}} = \frac{2}{\eta_F} \tag{13}$$

It can be found that the performance improvement does not depend on excitation level (V_{OC}), but η_F. Hence, we need to increase L or decrease C_P or R to obtain a higher performance from a SSHI circuit. The inductance L can be increased in a wide range of inductor selections; however, the DC resistance on an inductor should always be considered since larger L in a given volume usually introduces higher DC resistance. The resistance R can be decreased from the inductor selection and the design of the circuits, especially the analogue switches controlling the inductor shown in Fig. 2b. The C_P is the inherent capacitance of the PT; hence, it can only be deceased during MEMS design.

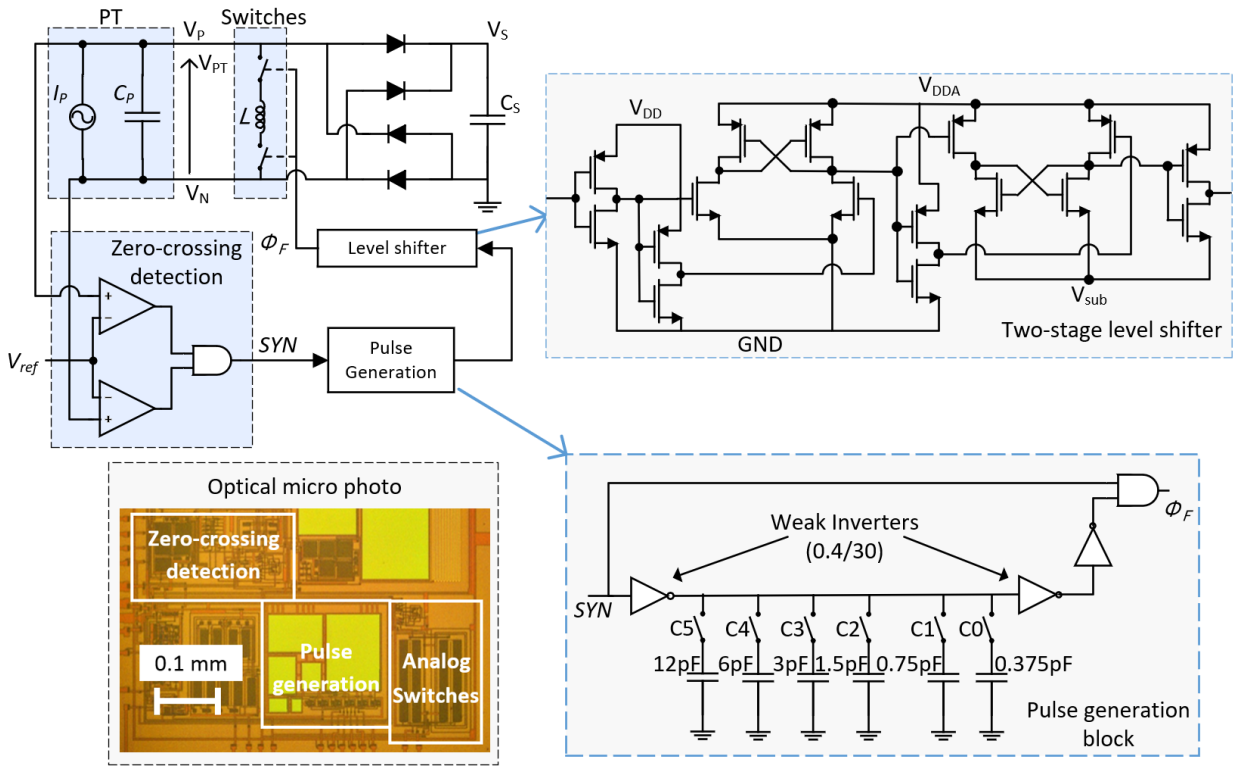

Fig. 3: SSHI circuit system architecture and circuit implementations.

III. SSHI Circuit Implementations

This section presents the circuit implementation of a SSHI rectifier and the system architecture is shown in Fig. 3, which consists of a zero-crossing detection block, a pulse generation block and two analog switches. The analogue switches are built with transistors of size 1500 µm/0.5 µm. The full bridge rectifier is formed by four off-chip Schottky diodes and the forward voltage drop is around $V_D \approx 0.3$ V. The zero-crossing block aims to find the zero-current moment of I_P, which is the right moment to flip V_{PT}. In order to find this moment, two continuous-time comparators are employed to compare the both electrodes of the PT, V_P and V_N, with a reference voltage V_{ref}. While I_P is close to zero, the diodes of the FBR are just about to turn OFF. At this moment, one of V_P and V_N is close to $-V_D$ and the other one is close to $V_S + V_D$. The reference voltage V_{ref} is set slightly higher than $-V_D$ to detect the moment while one of V_P and V_N leaves $-V_D$ and this is the moment while I_P is close to zero. In this work, V_{ref} is connected to the ground and this provides a good estimation of voltage flip moment. The outputs of the two comparators are ANDed and the signal SYN is a synchronous signal which consists of a rising edge at each zero I_P moment. A pulse signal ϕ_F is then generated according to each rising edge of SYN to control the analog switches to flip V_{PT}. The pulse of ϕ_F should be adjusted to be a half pseudo-period of the RLC oscillation system to achieve the maximum voltage flipping efficiency.

The pulse generation block aims to generate the fixed-width pulse signal, ϕ_F from SYN and the circuit diagram is shown in Fig. 3.This pulse generator is an AND gate where the signal SYN is ANDed with the delayed and inverted version of itself. The delay is achieved using two weak inverters charging up capacitors. The total capacitance formed by 6 on-chip capacitors can be adjusted by a 6-bit signal controlling the six switches C_5 to C_0. This 6-bit signal can be set externally to adjust the capacitance. The resulting pulse width of ϕ_F is adjustable over a range from 2 to 70 µs with step of 1.1 µs. With the help of this block, a pulse ϕ_F is generated with its pulsewidth adjusted to a half pseudo-period of the RLC oscillation loop, which approximately equals to $2\pi\sqrt{LC}$. This pulse signal then closes the RLC loop to flip the voltage V_{PT}. For a specific PT, this is a one-time configuration to match the generated pulsewidth with the half pseudo-period. When the PT is replaced by another PT with a different C_P capacitance, the 6-bit signal needs to be externally configured again since the half pseudo-period with this new PT is different. After the one-time adjustment is done, the capacitor array does not need to be configured again as long as the same PT is employed. However, due to the voltage and temperature variations, the generated pulsewidth with this configuration may vary to cause a slight mismatching with the half pseudo-period. In this case, performance will be degraded with a lower voltage flip efficiency. When the system is at the cold state, the SSHI rectifier is not operational due to the lack of a V_{DD} supply. The rectifier simply works as a passive FBR until the storage capacitor, C_S, is charged to a certain voltage level to provide a stable DC supply to the autonomous energy harvesting system. Once a V_{DD} is available, the SSHI rectifier starts operating.

The next section presents the design and the modeling of a piezoelectric energy harvester in MEMS process, which is

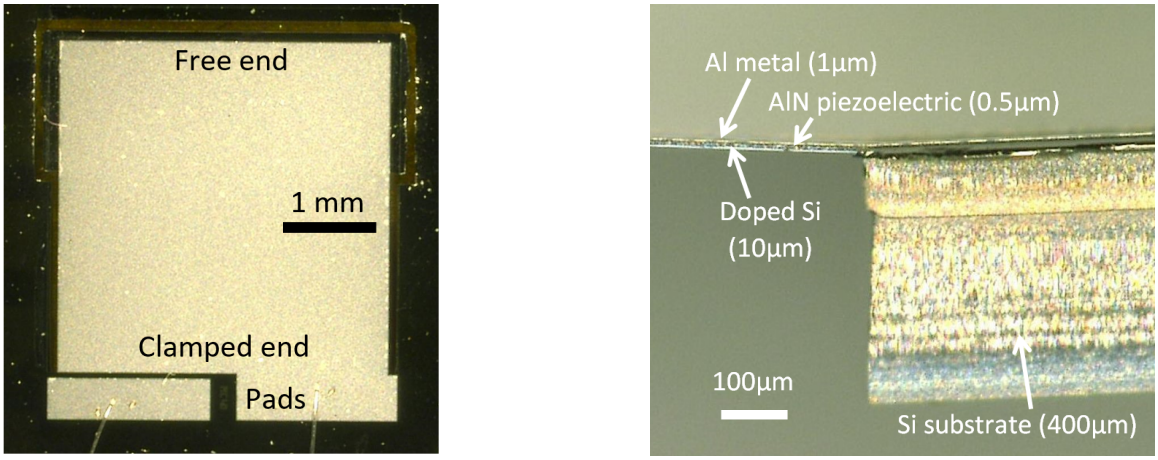

(a) (b)

Fig. 4: (a) Optical microphoto of MEMS transducer. (b) Cross-section of the MEMS process showing different layers.

integrated with the CMOS SSHI circuit in following experiments for power measurements. The SSHI is designed and fabricated in $0.35\,\mu\mathrm{m}$ HV CMOS process and the optical die photo is shown in Fig. 3. The active area of the SSHI circuit is around $0.15\,\mathrm{mm}^2$.

IV. MEMS VIBRATION ENERGY HARVESTER

The MEMS vibration energy harvester employed for the integration was an in-house device developed using the classical plain cantilever topology and an AlN (aluminium nitride) on SOI (silicon on insulator) process.

The FEA (finite element analysis) simulation of the $3.5\,\mathrm{mm}$ wide and long cantilever design is shown in figures 5a to 5c. The natural frequency of the micro-cantilever, where $50\,\%$ of the beam length is occupied up by proof mass, is predicted at $202\,\mathrm{Hz}$ as shown in figure 5a.

The micro-cantilevers can be driven to experience approximately $20\,\mathrm{MPa}$ of peak stress at $10\,\mathrm{g}$ of acceleration loading on the proof mass and exhibiting a peak displacement amplitude of about $70\,\mu\mathrm{m}$ as shown in figure 5b. This level of shuttle travel is relatively large for typical MEMS oscillators, which requires a deep cavity chip carrier to accommodate the silicon device. The induced stress across the beam length is shown in figure 5c

The MEMS fabrication process is shown in Fig. 5d. The fabricated devices were made up of a stack of materials consisting of: $10\,\mu\mathrm{m}$ thick doped silicon as the device layer with $0.5\,\mu\mathrm{m}$ thick AlN piezoelectric layer on top and a further $1\,\mu\mathrm{m}$ thick Al top electrode layer on top of AlN. The proof mass was achieved using un-etched regions of the $400\,\mu\mathrm{m}$ thick silicon handle wafer underneath the device silicon. The device is placed in a custom laser-cut, leadless chip carrier for testing.

Due to the thin substrate layer ($10\,\mu\mathrm{m}$) and its ceramic material (Silicon), the MEMS PT is very fragile at high excitation levels, especially at its resonant frequency. This limits its peak output power, which will be shown in the Section V. However, the small size makes it suitable to be co-integrated in a miniaturized system, such as the nail-size energy harvesting system proposed in this paper. With the high-efficiency SSHI interface circuit, the output power is significantly increased to compensate the drawback due to low excitation tolerance. This system can be employed to power wireless sensors, which are implemented where vibration excitation level is low.

V. EXPERIMENTS

This section presents the measured output power of the MEMS cantilevered PT with a resistive load, a full-bridge rectifier (FBR) and a SSHI circuit. First, the mechanical specifications, optimal resistive load and AC output power consumed in a matched resistive load are measured. The cantilevered MEMS PT is assembled into a custom laser-cut leadless chip carrier (LCC44); the chip carrier and the MEMS cantilever are shown in Fig. 1b. During the measurements, the chip carrier containing the PT is placed on a shaker excited at the natural frequency of the PT. In order to measure the AC output power consumed in a impedance-matched resistive load, the natural frequency should first be found. Fig. 6a shows the measured open-circuit voltage amplitude, noted as V_{OC}, over a range of excitation frequencies. From this figure, the natural frequency of the micro cantilever is found to be around $199\,\mathrm{Hz}$. After finding the natural frequency, the PT is then excited at its resonance and connected to a variable resistor to find the optimal resistive load matching the internal impedance of the PT. The power consumed in the variable resistor is calculated and the results are shown in Fig. 6b. The resistance is swept from $100\,\mathrm{k}\Omega$ to $600\,\mathrm{k}\Omega$ and the AC power is found to attain its peak while the load is at around $260\,\mathrm{k}\Omega$. Then, the load resistor is kept at $260\,\mathrm{k}\Omega$ by changing the excitation level to find the AC output power under different excitation levels. The results are shown in Fig. 6c and the maximum AC output power is found to be $22.1\,\mu\mathrm{W}$ at $3\,\mathrm{m/s}^2$.

The MEMS PT is then integrated with a FBR and a SSHI circuit to measure the rectified DC power. The FBR is implemented with four off-chip Schottky diodes and the SSHI circuit is implemented in a CMOS process. The forward voltage drop of the diode is measured at around $0.2\,\mathrm{V}$. Fig. 7 shows the measured waveforms of signals V_{PT}, SYN and

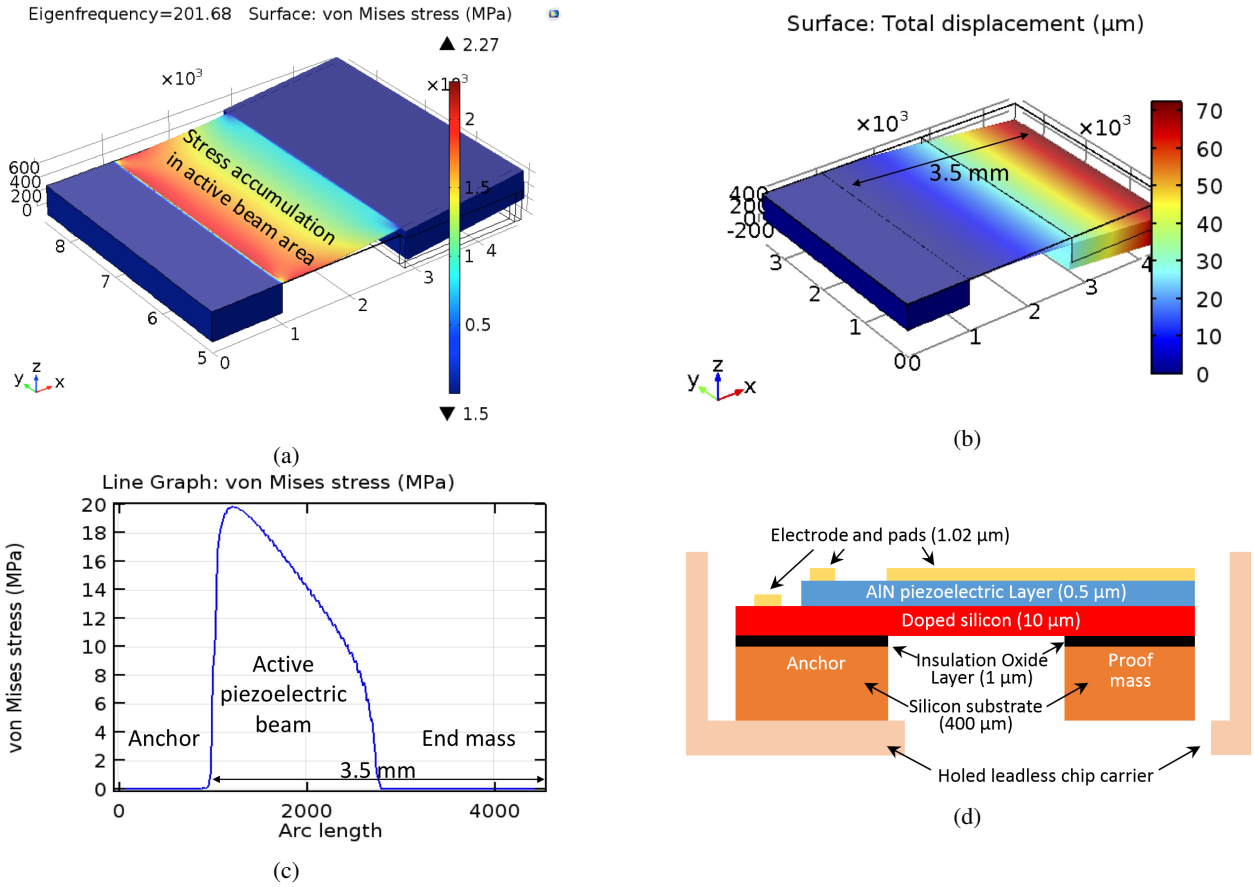

Fig. 5: (a) Fundamental resonant frequency, 202 Hz, for the micro-cantilever (3.5 mm square) where 50 % of the beam length is occupied by proof mass. (b) Peak displacement of 70 µm for the micro-cantilevers when driven to a peak stress of 20 MPa with 10 g response acceleration loading on the proof mass. (c) Induced stress distribution along the cantilever length. (d) A cantilevered MEMS PT with MEMS process showing different layers with corresponding thickness.

ϕ_F while using the FBR and using the SSHI circuit with three different inductor values. While using a passive FBR, the voltage V_{PT} is slowly flipped by the generated energy to overcome the thresholds. In this case, most of generated energy is wasted and only the energy while the V_{PT} attains its top and bottom limits can be extracted. In the following three figures, the SSHI circuit is employed with different inductor values. It can be seen that the voltage V_{PT} is correctly flipped for this half period and the signal SYN is synchronously generated to flip V_{PT}. While using an inductor with higher inductance, the voltage flipping efficiency is increased, which has been studied in equation (9).

Fig. 8a shows the output power under a given excitation level while varying the output DC voltage V_S, which is the voltage across the energy storage capacitor C_S connected at the output of the FBR and the SSHI circuit. During the measurements, the excitation level is $1.2\,\mathrm{m/s^2}$, which corresponds to an open-circuit voltage amplitude at $V_{OC} = 2\,\mathrm{V}$. Under this excitation level, the FBR can achieve its MPP (maximum power point) while $V_S = 0.9\,\mathrm{V}$ and the peak power is $1.8\,\mu\mathrm{W}$. While integrating the SSHI circuit with a $0.1\,\mathrm{mH}$ inductor, the peak power is increased to $6.2\,\mu\mathrm{W}$ when $V_S = 3\,\mathrm{V}$. The peak output power achieves $8.8\,\mu\mathrm{W}$, $11.6\,\mu\mathrm{W}$ and $14.1\,\mu\mathrm{W}$ while the inductor is chosen at $220\,\mu\mathrm{H}$, $470\,\mu\mathrm{H}$ and $1\,\mathrm{mH}$, respectively. Compared with the performance using a FBR, the output power while integrating the SSHI with the MEMS energy harvester is increased by $3.4\times$, $4.9\times$, $6.4\times$ and $7.8\times$, respectively, under the $1.2\,\mathrm{m/s^2}$ excitation with a $1\,\mathrm{mH}$ inductor. According to the performance improvement equation obtained in (13), the voltage flip loss ratios for these four inductor values can be calculated as $\eta_{0.1\,\mathrm{mH}} \approx 0.59$, $\eta_{0.22\,\mathrm{mH}} \approx 0.41$, $\eta_{0.47\,\mathrm{mH}} \approx 0.31$ and $\eta_{1\,\mathrm{mH}} \approx 0.25$, respectively. Comparing with the waveforms obtained in Fig. 7, the measured voltage flip losses for different inductor values approximately match the theoretical values obtained with (13).

Fig. 8b shows the output power under a range of excitation levels up to $3\,\mathrm{m/s^2}$, which corresponds to an open-circuit voltage of $V_{OC} = 5.2\,\mathrm{V}$. During the measurements, the output voltage is fixed at $V_S = 4\,\mathrm{V}$. From the results, it can be seen that the FBR can only extract energy under high excitation levels from $2.5\,\mathrm{m/s^2}$ as it sets a high threshold due to the high V_S value. Hence, the maximum output power while using a FBR is only $7\,\mu\mathrm{W}$. While the SSHI circuit is employed, the output power is significantly increased to $32\,\mu\mathrm{W}$ with a $100\,\mu\mathrm{H}$ inductor. This value is further increased to $40.6\,\mu\mathrm{W}$ with a $1\,\mathrm{mH}$ inductor due to higher voltage flipping efficiency.

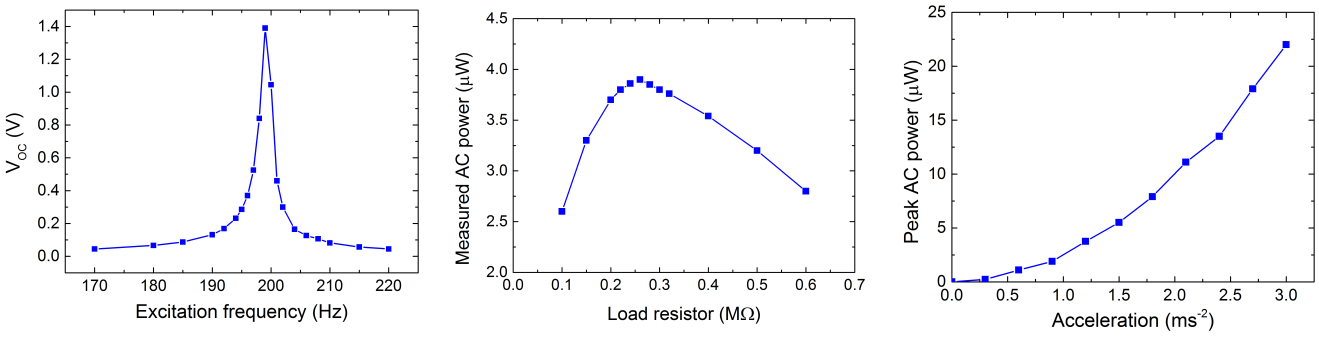

(a) (b) (c)

Fig. 6: (a) Measured open-circuit voltage amplitude. (b) Measured output power in different resistive loads ($V_{OC} = 2\,\mathrm{V}$). (c) Measured AC peak power consumed in a $260\,\mathrm{K\Omega}$ resistive load.

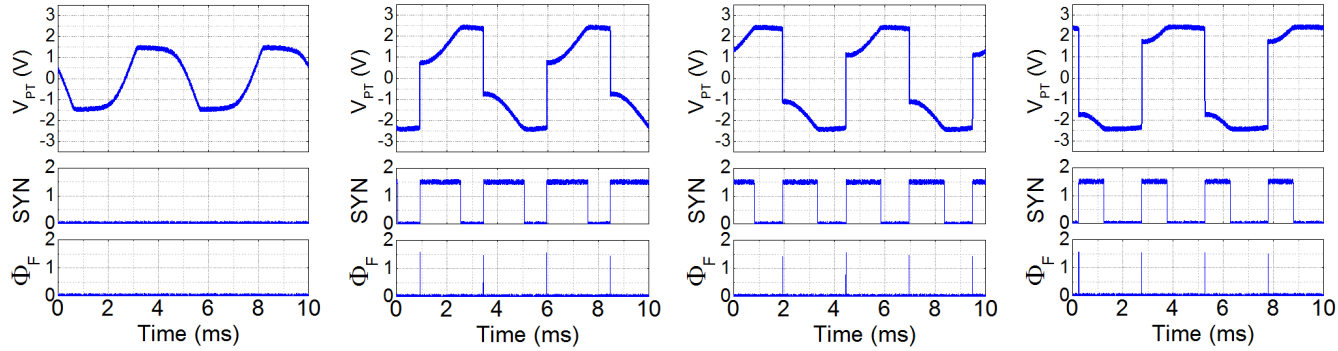

(a) (b) (c) (d)

Fig. 7: (a) Full-bridge rectifier ($V_{OC} = 2.5\,\mathrm{V}$, $V_S = 1\,\mathrm{V}$). (b) SSHI circuit with $100\,\mu\mathrm{H}$ inductor ($V_{OC} = 2\,\mathrm{V}$, $V_S = 2\,\mathrm{V}$). (c) SSHI circuit with $220\,\mu\mathrm{H}$ inductor ($V_{OC} = 2\,\mathrm{V}$, $V_S = 2\,\mathrm{V}$). (d) SSHI circuit with $1000\,\mu\mathrm{H}$ inductor ($V_{OC} = 2\,\mathrm{V}$, $V_S = 2\,\mathrm{V}$).

Therefore, the SSHI circuit improves the energy extraction performance by $5.8\times$ compared to the FBR.

Table I compares the work presented in this paper with prior publications. The second column shows the techniques used in each work and the following columns show the piezoelectric transducers used in experiments, operating frequency, internal capacitance of PTs, peak output power and the volume of PTs, respectively. The last column shows the power density ($\mathrm{mW/cm^3}$) by dividing the peak output power by the PT size. According to the table, the proposed the work presented in this paper shows the highest power density at $8.12\,\mathrm{mW/cm^3}$, which is higher than all other prior cited works. The high power density is achieved due to the custom MEMS PT and the highly efficient SSHI interface circuit. The compact design of the energy harvesting system also allows it to be implemented in miniaturized self-powered systems.

VI. Conclusion

This paper presents the integration of a MEMS piezoelectric energy harvester and a CMOS SSHI interface circuit to provide a peak DC output power of $40.6\,\mu\mathrm{W}$ with a record power density at $8.12\,\mathrm{mW/cm^3}$. The piezoelectric transducer (PT) is fabricated in a MEMS process with AlN as the piezoelectric material and the CMOS circuit is implemented in a $0.35\,\mu\mathrm{m}$ HV (high-voltage) CMOS process. Due to the integration of a MEMS PT and a CMOS circuit, the overall system volume of an energy harvesting system can be significantly decreased to sub-$\mathrm{cm^3}$ scale including all off-chip components. In addition, with the MEMS PT and the CMOS circuit, the measured DC output power is as high as $40.6\,\mu\mathrm{W}$ with the power improvement of $5.8\times$ compared to a passive FBR. This demonstration shows a pathway towards miniaturized vibration-powered wireless sensor solutions as an enabling technology for the Internet of things paradigm.

References

[1] R. J. M. Vullers, R. van Schaijk, I. Doms, C. Van Hoof, and R. Mertens, "Micropower energy harvesting," *Solid-State Electronics*, vol. 53, no. 7, pp. 684–693, 2009.

[2] P. D. Mitcheson, E. M. Yeatman, G. K. Rao, A. S. Holmes, and T. C. Green, "Energy harvesting from human and machine motion for wireless electronic devices," *Proceedings of the IEEE*, vol. 96, no. 9, pp. 1457–1486, 2008.

[3] S. Du, Y. Jia, C. Zhao, S.-T. Chen, and A. A. Seshia, "Real-world evaluation of a self-startup sshi rectifier for piezoelectric vibration energy harvesting," *Sensors and Actuators A: Physical*, vol. 264, pp. 180–187, 2017.

[4] A. Varpula, S. J. Laakso, T. Havia, J. Kyynrinen, and M. Prunnila, "Harvesting vibrational energy using material work functions," *Scientific Reports*, vol. 4, p. 6799, 2014.

[5] N. Rezaei-Hosseinabadi, A. Tabesh, and R. Dehghani, "A topology and design optimization method for wideband piezoelectric wind energy harvesters," *IEEE Transactions on Industrial Electronics*, vol. 63, no. 4, pp. 2165–2173, 2016.

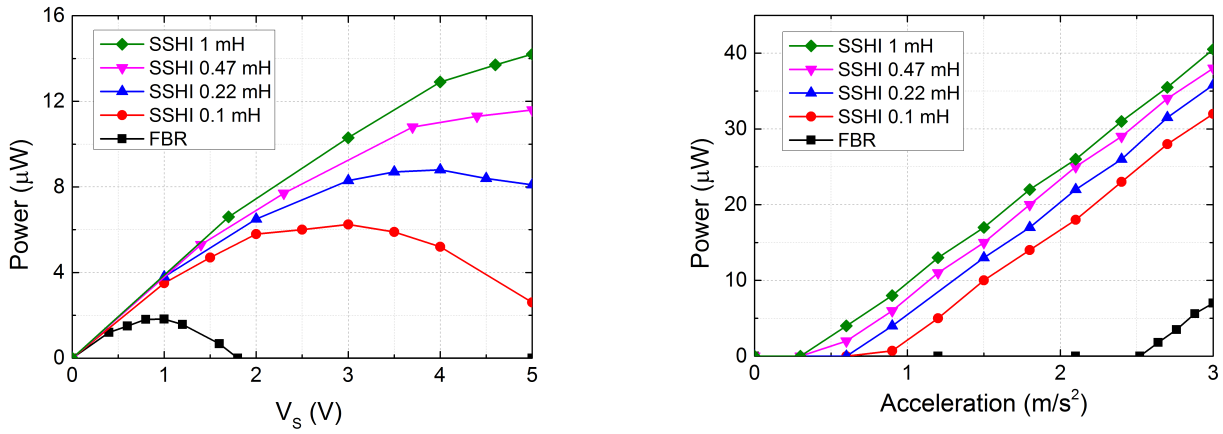

(a) (b)

Fig. 8: (a) Measured output power using FBR and SSHI circuits with different inductor values in a range of V_S values with $V_{OC} = 2\,\mathrm{V}$. (b) Measured output power using FBR and SSHI circuits with different inductor values in a range of excitation levels from $0\,\mathrm{m/s^2}$ to $3\,\mathrm{m/s^2}$ with $V_S = 4\,\mathrm{V}$.

TABLE I: Performance comparison with state-of-the-art

Reference	Technique	Piezoelectric transducer	Frequency	Piezoelectric capacitance	Peak power	Performance over FBR	PT size	Power density
[42]	SSHI	Mide V22B	225 Hz	18 nF	68 μW	4×	0.185 $\mathrm{cm^3}$	0.37 $\mathrm{mW/cm^3}$
[34]	SSHC	Mide V21BL	92 Hz	45 nF	1.2 mW	2.7× − 9.7×	0.59 $\mathrm{cm^3}$	2 $\mathrm{mW/cm^3}$
[53]	PSCE	Mide V22B	173 Hz	19.5 nF	477 μW	2.1×	0.185 $\mathrm{cm^3}$	2.58 $\mathrm{mW/cm^3}$
[49]	SSHI	Custom MEMS	155 Hz	8.5 nF	95 μW	2.5×	0.027 $\mathrm{cm^3}$	3.5 $\mathrm{mW/cm^3}$
[32]	SSHI	Mide V22B	134 Hz	26 nF	500 μW	4.4×	0.185 $\mathrm{cm^3}$	2.7 $\mathrm{mW/cm^3}$
This work	SSHI	Custom MEMS	199 Hz	2.82 nF	40.6 μW	5.8×	0.005 $\mathrm{cm^3}$	8.12 $\mathrm{mW/cm^3}$

[6] M. Belleville, H. Fanet, P. Fiorini, P. Nicole, M. J. M. Pelgrom, C. Piguet, R. Hahn, C. Van Hoof, R. Vullers, M. Tartagni, and E. Cantatore, "Energy autonomous sensor systems: Towards a ubiquitous sensor technology," *Microelectronics Journal*, vol. 41, no. 11, pp. 740–745, 2010.

[7] S. Roundy and P. K. Wright, "A piezoelectric vibration based generator for wireless electronics," *Smart Materials and Structures*, vol. 13, no. 5, p. 1131, 2004.

[8] S. Niu, X. Wang, F. Yi, Y. S. Zhou, and Z. L. Wang, "A universal self-charging system driven by random biomechanical energy for sustainable operation of mobile electronics," *Nat Commun*, vol. 6, 2015.

[9] S. Du, Y. Jia, and A. A. Seshia, "Piezoelectric vibration energy harvesting: A connection configuration scheme to increase operational range and output power," *Journal of Intelligent Material Systems and Structures*, p. 1045389X16682846, 2016.

[10] S. P. Beeby, M. J. Tudor, and N. M. White, "Energy harvesting vibration sources for microsystems applications," *Measurement Science and Technology*, vol. 17, no. 12, p. R175, 2006.

[11] A. Harb, "Energy harvesting: State-of-the-art," *Renewable Energy*, vol. 36, no. 10, pp. 2641–2654, 2011.

[12] G. Tang, B. Yang, J.-q. Liu, B. Xu, H.-y. Zhu, and C.-s. Yang, "Development of high performance piezoelectric d33 mode mems vibration energy harvester based on pmn-pt single crystal thick film," *Sensors and Actuators A: Physical*, vol. 205, no. 0, pp. 150–155, 2014.

[13] J. Lee and B. Choi, "Development of a piezoelectric energy harvesting system for implementing wireless sensors on the tires," *Energy Conversion and Management*, vol. 78, no. 0, pp. 32–38, 2014.

[14] A. Khaligh, Z. Peng, and Z. Cong, "Kinetic energy harvesting using piezoelectric and electromagnetic technologies - state of the art," *IEEE Transactions on Industrial Electronics*, vol. 57, no. 3, pp. 850–860, 2010.

[15] S. Du, G. A. J. Amaratunga, and A. A. Seshia, "A cold-startup sshi rectifier for piezoelectric energy harvesters with increased open-circuit voltage," *IEEE Transactions on Power Electronics*, vol. 34, no. 1, pp. 263–274, 2019.

[16] H. S. Kim, J.-H. Kim, and J. Kim, "A review of piezoelectric energy harvesting based on vibration," *International journal of precision engineering and manufacturing*, vol. 12, no. 6, pp. 1129–1141, 2011.

[17] R. Yuan and D. P. Arnold, "An input-powered vibrational energy harvesting interface circuit with zero standby power," *Power Electronics, IEEE Transactions on*, vol. 26, no. 12, pp. 3524–3533, 2011.

[18] J. Liang and W.-H. Liao, "Improved design and analysis of self-powered synchronized switch interface circuit for piezoelectric energy harvesting systems," *IEEE Transactions on Industrial Electronics*, vol. 59, no. 4, pp. 1950–1960, 2012.

[19] L. M. Miller, A. D. T. Elliott, P. D. Mitcheson, E. Halvorsen, I. Paprotny, and P. K. Wright, "Maximum performance of piezoelectric energy harvesters when coupled to interface circuits," *IEEE Sensors Journal*, vol. 16, no. 12, pp. 4803–4815, 2016.

[20] G. D. Szarka, B. H. Stark, and S. G. Burrow, "Review of power conditioning for kinetic energy harvesting systems," *Power Electronics, IEEE Transactions on*, vol. 27, no. 2, pp. 803–815, 2012.

[21] S. Du, Y. Jia, C. Zhao, G. A. J. Amaratunga, and A. A. Seshia, "A passive design scheme to increase the rectified power of piezoelectric energy harvesters," *IEEE Transactions on Industrial Electronics*, vol. 65, no. 9, pp. 7095–7105, 2018.

[22] Q. Shi, T. Wang, and C. Lee, "Mems based broadband piezoelectric ultrasonic energy harvester (pueh) for enabling self-powered implantable biomedical devices," vol. 6, p. 24946, 2016.

[23] K. Wasa, T. Matsushima, H. Adachi, I. Kanno, and H. Kotera, "Thin-film piezoelectric materials for a better energy harvesting mems," *Microelectromechanical Systems, Journal of*, vol. 21, no. 2, pp. 451–457, 2012.

[24] H. Liu, C. Lee, T. Kobayashi, C. J. Tay, and C. Quan, "Piezoelectric mems-based wideband energy harvesting systems using a frequency-up-conversion cantilever stopper," *Sensors and Actuators A: Physical*, vol. 186, no. 0, pp. 242–248, 2012.

[25] L. C. J. Blystad, E. Halvorsen, and S. Husa, "Piezoelectric mems energy harvesting systems driven by harmonic and random vibrations," *Ultrasonics, Ferroelectrics, and Frequency Control, IEEE Transactions on*, vol. 57, no. 4, pp. 908–919, 2010.

[26] G. D. Szarka, S. G. Burrow, and B. H. Stark, "Ultralow power, fully autonomous boost rectifier for electromagnetic energy harvesters," *IEEE Transactions on Power Electronics*, vol. 28, no. 7, pp. 3353–3362, 2013.

[27] Y. Jia, S. Du, and A. A. Seshia, "Micromachined cantilevers-on-membrane topology for broadband vibration energy harvesting," *Journal of Micromechanics and Microengineering*, vol. 26, no. 12, p. 124007, 2016.

[28] X.-D. Do, H.-H. Nguyen, S.-K. Han, D. S. Ha, and S.-G. Lee, "A self-powered high-efficiency rectifier with automatic resetting of transducer capacitance in piezoelectric energy harvesting systems," *Very Large Scale Integration (VLSI) Systems, IEEE Transactions on*, vol. 23, no. 3, pp. 444–453, 2015.

[29] D. Kwon and G. A. Rincon-Mora, "A single-inductor 0.35 um cmos energy-investing piezoelectric harvester," *IEEE Journal of Solid-State Circuits*, vol. 49, no. 10, pp. 2277–2291, 2014.

[30] G. Shi, Y. Xia, Y. Ye, L. Qian, and Q. Li, "An efficient self-powered synchronous electric charge extraction interface circuit for piezoelectric energy harvesting systems," *Journal of Intelligent Material Systems and Structures*, p. 1045389X15624796, 2016.

[31] Y. Jia, S. Du, and A. A. Seshia, "Twenty-eight orders of parametric resonance in a microelectromechanical device for multi-band vibration energy harvesting," *Scientific Reports*, vol. 6, p. 30167, 2016.

[32] D. A. Sanchez, J. Leicht, F. Hagedorn, E. Jodka, E. Fazel, and Y. Manoli, "A parallel-sshi rectifier for piezoelectric energy harvesting of periodic and shock excitations," *IEEE Journal of Solid-State Circuits*, vol. 51, no. 12, pp. 2867–2879, 2016.

[33] L. Wu, X. D. Do, S. G. Lee, and D. S. Ha, "A self-powered and optimal sshi circuit integrated with an active rectifier for piezoelectric energy harvesting," *IEEE Transactions on Circuits and Systems I: Regular Papers*, vol. 64, no. 3, pp. 537–549, 2017.

[34] S. Du and A. A. Seshia, "An inductorless bias-flip rectifier for piezoelectric energy harvesting," *IEEE Journal of Solid-State Circuits*, vol. 52, no. 10, pp. 2746–2757, 2017.

[35] J. Sankman and M. Dongsheng, "A 12-uw to 1.1-mw aim piezoelectric energy harvester for time-varying vibrations with 450-na iq," *Power Electronics, IEEE Transactions on*, vol. 30, no. 2, pp. 632–643, 2015.

[36] H. Shen, H. Ji, J. Qiu, Y. Bian, and D. Liu, "Adaptive synchronized switch harvesting: A new piezoelectric energy harvesting scheme for wideband vibrations," *Sensors and Actuators A: Physical*, vol. 226, pp. 21–36, 2015.

[37] S. Javvaji, V. Singhal, V. Menezes, R. Chauhan, and S. Pavan, "Analysis and design of a multi-step bias-flip rectifier for piezoelectric energy harvesting," *IEEE Journal of Solid-State Circuits*, pp. 1–11, 2019.

[38] S. Du, Y. Jia, C. Zhao, G. A. J. Amaratunga, and A. A. Seshia, "A fully integrated split-electrode sshc rectifier for piezoelectric energy harvesting," *IEEE Journal of Solid-State Circuits*, vol. 54, no. 6, pp. 1733–1743, 2019.

[39] S. Chamanian, A. Muhtaroglu, and H. Kulah, "A self-adapting synchronized-switch interface circuit for piezoelectric energy harvesters," *IEEE Transactions on Power Electronics*, pp. 1–1, 2019.

[40] Z. J. Chew and M. Zhu, "Adaptive self-configurable rectifier for extended operating range of piezoelectric energy harvesting," *IEEE Transactions on Industrial Electronics*, pp. 1–1, 2019.

[41] G. Shi, Y. Xia, H. Xia, X. Wang, L. Qian, Z. Chen, Y. Ye, and Q. Li, "An efficient power management circuit based on quasi maximum power point tracking with bidirectional intermittent adjustment for vibration energy harvesting," *IEEE Transactions on Power Electronics*, vol. 34, no. 10, pp. 9671–9685, 2019.

[42] Y. K. Ramadass and A. P. Chandrakasan, "An efficient piezoelectric energy harvesting interface circuit using a bias-flip rectifier and shared inductor," *IEEE Journal of Solid-State Circuits*, vol. 45, no. 1, pp. 189–204, 2010.

[43] S. Du, Y. Jia, and A. A. Seshia, "An efficient inductorless dynamically configured interface circuit for piezoelectric vibration energy harvesting," *IEEE Transactions on Power Electronics*, vol. 32, no. 5, pp. 3595–3609, 2017.

[44] E. Lefeuvre, A. Badel, A. Brenes, S. Seok, M. Woytasik, and C. S. Yoo, "Analysis of piezoelectric energy harvesting system with tunable sece interface," *Smart Materials and Structures*, vol. 26, no. 3, p. 035065, 2017.

[45] K. Dongwon and G. A. Rincon-Mora, "A single-inductor ac-dc piezoelectric energy-harvester/battery-charger ic converting (0.35 to 1.2v) to (2.7 to 4.5v)," in *Solid-State Circuits Conference Digest of Technical Papers (ISSCC), 2010 IEEE International*, Conference Proceedings, pp. 494–495.

[46] S. Du, Y. Jia, C. D. Do, and A. A. Seshia, "An efficient sshi interface with increased input range for piezoelectric energy harvesting under variable conditions," *IEEE Journal of Solid-State Circuits*, vol. 51, no. 11, pp. 2729–2742, 2016.

[47] M. Dini, A. Romani, M. Filippi, and M. Tartagni, "A nanopower synchronous charge extractor ic for low-voltage piezoelectric energy harvesting with residual charge inversion," *IEEE Transactions on Power Electronics*, vol. 31, no. 2, pp. 1263–1274, 2016.

[48] P. Gasnier, J. Willemin, S. Boisseau, G. Despesse, C. Condemine, G. Gouvernet, and J. J. Chaillout, "An autonomous piezoelectric energy harvesting ic based on a synchronous multi-shot technique," *IEEE Journal of Solid-State Circuits*, vol. 49, no. 7, pp. 1561–1570, 2014.

[49] E. E. Aktakka and K. Najafi, "A micro inertial energy harvesting platform with self-supplied power management circuit for autonomous wireless sensor nodes," *IEEE Journal of Solid-State Circuits*, vol. 49, no. 9, pp. 2017–2029, 2014.

[50] S. Du and A. A. Seshia, "A fully integrated split-electrode synchronized-switch-harvesting-on-capacitors (se-sshc) rectifier for piezoelectric energy harvesting with between 358enhancement," in *2018 IEEE International Solid - State Circuits Conference - (ISSCC)*, Conference Proceedings, pp. 152–154.

[51] L. Wu and D. S. Ha, "A self-powered piezoelectric energy harvesting circuit with an optimal flipping time sshi and maximum power point tracking," *IEEE Transactions on Circuits and Systems II: Express Briefs*, pp. 1–1, 2019.

[52] L. Cheng, W. Ki, Y. Lu, and T. Yim, "Adaptive on/off delay-compensated active rectifiers for wireless power transfer systems," *IEEE Journal of Solid-State Circuits*, vol. 51, no. 3, pp. 712–723, March 2016.

[53] T. Hehn, F. Hagedorn, D. Maurath, D. Marinkovic, I. Kuehne, A. Frey, and Y. Manoli, "A fully autonomous integrated interface circuit for piezoelectric harvesters," *IEEE Journal of Solid-State Circuits*, vol. 47, no. 9, pp. 2185–2198, 2012.

Sijun Du (S'14−M'17) received a First Class in B.Eng degree in Electronic Engineering from University Pierre and Marie Curie (UPMC, Sorbonne University), Paris, France, in 2011, a Distinction in M.Sc degree in Electrical and Electronic Engineering from Imperial College, London, U.K., in 2012. He started his Ph.D research in October 2014 and obtained the Ph.D degree in engineering from University of Cambridge, Cambridge, U.K. in 2017. He joined the Berkeley Wireless Research Center (BWRC), Department of Electrical Engineering and Computer Sciences (EECS) at University of California, Berkeley, CA, 94720, U.S.A. in April 2018, where he is currently a post-doctoral scholar.

He worked at the Laboratory Laboratoire d'Informatique de Paris 6 (LIP6), University Pierre and Marie Curie, Paris, France, and then worked as a digital IC engineer in Shanghai, China, between 2012 and 2014. He was with the Cambridge Nanoscience Centre at University of Cambridge for his Ph.D research between 2014 and 2017. He was an engineer intern at Qualcomm Technology Inc., San Diego, California, U.S.A. between August 2016 and November 2016. He was a visiting scholar at the Brain-Chip Research Center (BCRC), Department of Microelectronics, Fudan University, Shanghai, China, between December 2017 and March 2018.

His research interests include energy harvesters and associated interfaces, energy conversion circuits and systems, power electronics, power management circuits, rectification circuits, wireless communication circuits.

Yu Jia (S'13−M'14−SM'19) received a First Class (Honours) in MEng Electromechanical Engineering from the University of Southampton in 2010, and PhD in Engineering from the University of Cambridge in 2014. He was then a Research Associate at Cambridge for a year before joining the faculty at University of Chester as Lecturer in 2015, Senior Lecturer in 2017 and Associate Professor in 2019. He is currently a Senior Lecturer in Mechanical Engineering at the Aston University. His research interests include vibration energy harvesting, microelectromechanical systems (MEMS), nonlinear vibration dynamics, smart composites and smart integrated systems. He is a co-founder of 8power Ltd., a senior member of IEEE and is a steering board member of the Energy Harvesting Network.

Chun Zhao (S'14−M'16) received B.Eng. degree in measurement and control technology and instrument from the Huazhong University of Science and Technology, Wuhan, China, in 2009; M.Sc. degree in analog and digital IC design from Imperial College London, London, U.K., in 2011; and Ph.D. degree in microelectromechanical systems (MEMS) from the University of Southampton, Southampton, U.K., in 2016.

From April 2015 to March 2016, he was a full time Research Scientist at Sharp Laboratories of Europe, Oxford, U.K., working on the research and development of MEMS acoustic devices and integrated control circuit based on TFT. From April 2016 to August 2018, he was with the Department of Engineering, University of Cambridge, where he worked as a Research Associate in MEMS, focusing on MEMS resonant accelerometers and its low noise front-end electronics. He joined the School of Physics, Huazhong University of Science and Technology, Wuhan, China in September 2018, where he is currently an associate professor.

He has authored or co-authored 30 journal and conference publications in the field of MEMS physical sensors, MEMS energy harvesters and interface electronics design. He has also served as an invited reviewer for journals including IEEE JMEMS, Elsevier Sensors and Actuators A: Physical, MDPI Sensors and Nature Microsystems & Nanoengineering.

His current research interests include MEMS, microresonators, miniature sensors (such as inertial sensors and other physical sensors) and actuators (including ultrasonic devices), energy harvesters, MEMS system modelling and circuit design.

Gehan A. J. Amaratunga received his BSc degree in Electronic Engineering and the IEE Prize for the best graduating student from Cardiff University, UK (1979) and PhD degree from University of Cambridge in 1983. Since receiving his PhD from Cambridge, he has held other academic and research positions at Southampton University, the University of Liverpool and Stanford University. Since 1998 he has held the 1966 Chair and Professorship in Engineering at the University of Cambridge. He is also Visiting Professor at Yunnan University and Peking University Graduate School, Shenzhen in China. He is a Fellow of the Royal Academy of Engineering, National Academy of Sciences of Sri Lanka, Royal Society of Arts and the Institution of Engineering and Technology (formerly the IEE). He has published over 600 archived academic papers and is an inventor on 45 granted patents. His research is in the broad area of materials and technologies for electrical energy and power. It intersects electrical and electronic engineering with chemistry, physics, materials science and information systems.

Ashwin A. Seshia (S'97−M'02−SM'10) received his BTech in Engineering Physics from IIT Bombay in 1996 and his MS and PhD degrees in Electrical Engineering and Computer Science from the University of California Berkeley in 1999 and 2002 respectively. He is presently the Professor of Microsystems Technology at Cambridge University. He is also a Fellow of Queens' College and a co-investigator of the Cambridge Centre for Smart Infrastructure and Construction. His research interests are in the domain of micro- and nano-engineered dynamical systems with applications to sensors and sensor systems. He is a Fellow of the Institute of Physics and a Fellow of the Institution of Engineering and Technology. Ashwin serves on the editorial boards of the IEEE Journal of Microelectromechanical systems and the IEEE Transactions on Ultrasonics, Ferroelectrics and Frequency Control.